Probabilistic characteristics of random damage events and their quantification in acrylic bone cement

Volume 21 · Number 11 · November 2010
ISSN 0957-4530

Materials in Medicine

Journal of Materials Science

jMS

Official publication
of the European Society
for Biomaterials

ESB

Available
online
www.springerlink.com

Springer

Springer

Springer

Probabilistic characteristics of random damage events and their quantification in acrylic bone cement

Gang Qi · Steven F. Wayne · Oliver Penrose · Gladius Lewis · John I. Hochstein · Kenneth A. Mann

Abstract The failure of brittle and quasi-brittle polymers can be attributed to a multitude of random microscopic damage modes, such as fibril breakage, crazing, and microfracture. As the load increases, new damage modes appear, and existing ones can transition into others. In the example polymer used in this study—a commercially available acrylic bone cement—these modes, as revealed by scanning electron microscopy of fracture surfaces, include nucleation of voids, cracking, and local detachment of the beads from the matrix. Here, we made acoustic measurements of the randomly generated microscopic events (RGME) that occurred in the material under pure tension and under three-point bending, and characterized the severity of the damage by the entropy (s) of the probability distribution of the observed acoustic signal amplitudes. We correlated s with the applied stress (σ) by establishing an empirical s–σ relationship, which quantifies the activities of RGME under Mode I stress. It reveals the state of random damage modes: when $ds/d\sigma > 0$, the number of damage modes present increases with increasing stress, whereas it decreases when $ds/d\sigma < 0$. When $ds/d\sigma \approx 0$, no new random damage modes occur. In the s–σ curve, there exists a transition zone, with the stress at the "knee point" in this zone (center of the zone) corresponding to ~ 30 and $\sim 35\%$ of the cement's tensile and bending strengths, respectively. This finding explains the effects of RGME on material fatigue performance and may be used to approximate fatigue limit.

1 Introduction

Random damage in components and structures, fabricated from brittle and quasi-brittle polymers, when loaded, has been extensively investigated using both experimental and theoretical methods [1–7]. As such, much is known about many aspects of this phenomenon in these materials. For example, (1) many random damage modes are recognized, among which are void nucleation, microfracture, crazing, fibril breakage and debonding [1, 2], fracture in craze development [1–5], and distributed microdamage with certain patterns [6, 7]; (2) the distribution of the random damage over the various modes changes as the stress increases; and (3) random damage occurs in the form of microscopic events with specific characteristics.

The type of failure in many of these brittle and quasi-brittle polymers is considered as brittle failure. It is reasonable to hypothesize that these materials are in a "damaged state" when they are subjected to load. Evidence of this damage state is the continuous occurrence of randomly generated microscopic damage as observed by many authors, as reviewed later. Knowledge is lacking, however, about the probabilistic characteristics of random damage events, and quantification of the evolution and severity of these events and their distribution over damage modes under increasing stress. Also, little is known about how the

G. Qi (✉) · S. F. Wayne · G. Lewis · J. I. Hochstein
Department of Mechanical Engineering,
University of Memphis, Memphis, TN 38152, USA
e-mail: gangqi@memphis.edu

O. Penrose
Department of Mathematics and the Maxwell Institute
for Mathematical Sciences, Heriot-Watt University,
Edinburgh EH14 4AS, Scotland, UK

K. A. Mann
Upstate Medical University, Syracuse, NY 13210, USA

S. F. Wayne
Propane Education and Research Council,
Washington, DC 20036, USA

modes of randomly generated microscopic events and the transition when a change of these damage modes occurs influence the mechanical performance of a polymeric component/structure.

The objectives of the present work were twofold. Firstly, to establish an experimental approach that involves the use of acoustic sensing to detect the occurrence of randomly generated microscopic events, and the use of scanning electron microscopy (SEM) to identify various damage modes and their occurrence at different stress levels in a brittle or quasi-brittle polymer. Secondly, to develop a theoretical approach that takes into account the influence of these randomly generated microscopic events on the material's macroscopic behavior under the applied stress. We used a poly methyl methacrylate (PMMA) bone cement (hereinafter referred to as "bone cement"), which is a quasi-brittle, two-component polymer, as the sample material to illustrate this new approach. There were two reasons for this choice. First, bone cements are widely used by surgeons for anchoring total joint replacements [8]. Thus, the mechanical properties of bone cement, which depend upon the random microscopic damage formed in the material under stress in vivo, are of obvious clinical importance. Second, most studies of bone cement have focused on particular modes of damage [9, 10], such as the propagation of microcracks [10, 11], fracture [12], and fatigue [13–16], rather than on the evolving process of randomly generated microscopic events.

2 Materials and methods

A commercially available bone cement brand, VersaBond™ (Smith & Nephew, Inc., Memphis, TN, USA), was used. The powder constituents are $18.0 \times g$ of beads of methyl methacrylate co-polymer, $20.0 \times g$ beads of methylmethacrylate homopolymer, $3.8 \times g$ of ZrO_2 particles, and $0.5 \times g$ of benzoyl peroxide, while the liquid monomer (MMA) constituents are 19.87 mL of methyl methacrylate (stabilized with hydroquinone) and 0.13 ml of dimethyl-*p*-toluidine.

2.1 Specimen fabrication method, study groups, loading types, and SEM examinations

The cement powder and liquid monomer were mixed by hand in a polymeric bowl open to the ambient laboratory air. The mixture was poured into a specimen mold and was left to cure in the mold for at least 48 h, then removed, and aged, with all these steps being carried out in air.

Three groups of specimens were studied: Group I, which was comprised of 21 rectangular cross-sectioned, dog-bone tension specimens (ASTM D638–98 Type IV specimens); Group II, which was comprised of 22 rectangular cross-

sectioned, three-point bend specimens (1200 mm × 10 mm × 10 mm), with loading span of 980 mm; and Group III, which was comprised of two Group II-type specimens for the purpose of SEM examination. Group I and II specimens were tested to rupture under tensile stress (in fracture mechanics, this is called Mode I failure). The nominal stress values in Group I and II specimens are defined as the ratio of the load to the cross-sectional area of the specimen and the maximum tensile stress, respectively. Since the shear stress in three-point bending contributes <4% to the principal stress, it was ignored.

Both the pure tension and three-point bending loading were performed using a screw-driven materials testing machine (Model 4465; Instron, Inc., Canton, PA), at a crosshead displacement rate of 1 mm/min. Groups I and II specimens were loaded continuously to fracture. Group III specimens were loaded to an intermediate load level of 92 N or 382 N and then the load was removed.

The microstructural examinations were of: (1) the surfaces of as-fabricated specimens that were notched, frozen in liquid nitrogen, and then fractured by hand to generate mirror, mist, and hackle surfaces [17]; (2) the surfaces of Groups I and II specimens following their fracture in the stress tests; and (3) the surfaces of Group III specimens which, after removal of the loading, were notched, frozen in liquid nitrogen, and then fractured by hand.

2.2 Acoustic emission (AE) tests

These tests were carried out in conjunction with the stress tests. The acoustic data were integrated with the load readings in such a way that when an AE signal exceeded the pre-determined threshold, the corresponding load level was read at the same time and at the same sampling rate. Acoustic signals from the damage events were observed by attaching four AE sensors (Nano 30; Physical Acoustics, Inc., Princeton, NJ, USA) to each test specimen. For each sensor, the resonant frequency was 140 kHz and the operating frequency range was 125–750 kHz. This type of sensor is known with sensitivity for the uses with bone cement specimens [18, 19]. The acoustic signals were exported from the sensors to a 40 dB pre-amplifier, whose band pass filter was between 2.5 kHz and 3.8 MHz (AEP4; Vallen-Systeme GmbH, Munich, Germany), and then to a multi-channel AE data processor (ASMY-5; Vallen-Systeme GmbH). To choose a signal threshold that would optimize the signal-to-noise ratio, the entire load train was tested first. There were no detectable acoustic signals at or below 35.5 dB; so, this was used as the threshold. The maximum amplitude observed in the tests was 93.8 dB. A computer program recorded the rate of arrival of signals in each of the ten equal sub-intervals 35.5–41.3, 41.3–47.2, 47.2–53.0, 53.0–58.8, 58.8–64.6, 64.6–70.5, 70.5–76.3,

76.3–82.1, 82.1–88.0, and 88.0–93.8 dB. For each value of the (increasing) stress we tabulated the cumulative number of acoustic events per unit volume (cm^3) in each sub-interval of acoustic intensity.

2.3 The probabilistic entropy of acoustic data

As a method of concisely characterizing the distribution of acoustic event amplitudes, we used probabilistic entropy, a choice that was motivated partly by the work of Garcimartin, et al. [20], although the definition of probabilistic entropy used here differs fundamentally from theirs. Our probabilistic entropy is a practical approach to assess the state of randomly generated microscopic events in a material from acoustic observations. We chose to base our approach on the shape of the distribution of acoustic event amplitudes rather than on the total number in that distribution, because, in addition to varying with the amount of damage, the latter parameter also depends significantly on other factors; for example, it is different for bending and for tension.

To characterize the shape of the distribution concisely, we have used an indicator based on the Gibbs formula [21],

$$S := \int_0^1 \rho(x) \ln(1/\rho(x)) dx \qquad (1)$$

for the entropy of a continuous probability distribution with density ρ. Let x denote the amplitude of an acoustic event, measured on a scale where $x = 0$ corresponds to 35.5 dB and $x = 1$ corresponds to 93.8 dB, so that in terms of x the ten sub-intervals used by the detector are $(0, 0.1)$, $(0.1, 0.2)$, …, $(0.9, 1)$. Suppose that the (scaled) amplitudes of the acoustic events are independent random variables distributed on the interval $(0, 1)$ with probability density $\rho(x)$; then the probability that one of these amplitudes, chosen at random, lies in the ith sub-interval is $p_i := \int_{0.1(i-1)}^{0.1i} \rho(x) dx$. We shall approximate the Gibbs formula by replacing $\rho(x)$ on each sub-interval of the x axis by its average over that sub-interval, which is $\rho_i := \frac{1}{0.1} \int_{0.1(i-1)}^{0.1i} \rho(x) dx = 10 p_i$. This gives the approximation

$$S \approx \sum_{i=1}^{10} 0.1 \rho_i \ln(1/\rho_i) = \sum_{i=1}^{10} p_i \ln(0.1/p_i). \qquad (2)$$

After N acoustic events have occurred, the expected number of events with amplitudes in the ith sub-interval is Np_i The observed number of events in that sub-interval, which we denote by n_i, is an estimate of Np_i and so $f_i := n_i/N$ is an estimate of p_i. The corresponding estimate for the above approximation to the entropy is $\sum_{i=1}^{10} f_i \ln(0.1/f_i)$. Thus, we have

$$S \approx s := \sum_{i=1}^{10} f_i \ln(0.1/f_i)$$

We shall use s as our indicator of the shape of the distribution. Its greatest possible value is zero, achieved when the observations are equally distributed over the ten sub-intervals (i.e. $f_i = 0.1$ for $i = 1, 2, … 10$). Its least possible value is $\ln 0.1 = -2.3$, achieved when all the observations fall in the same sub-interval.

Since acoustic data are obtained from fracture tests, the elastic stress/strain waves released are due to the creation of free faces of random damage crack formation and other microscopic events. Thus, the proposed entropy ties directly with the physical mechanisms of these waves. For instance, the amplitudes and counts of these electronic signals have been found to be proportional to the magnitude and quantity of the random microscopic events of the material as a consequence to the applied stress [23–27]. These literature results [23–27] allow us to assume that, statistically, each random damage mode would cover a certain range of acoustic event amplitudes. The more the different random damage modes are present, the more the observed amplitudes will be spread out over the available range, and so the larger will be the entropy. Thus, the entropy, as a macroscopic quantity defined by Eq. (2) gives a measure of the number of different modes that are acting, and can be used to reveal: (1) the state of the randomly generated damage modes; (2) the evolution of these modes; and (3) the severity of random damage formation.

3 Results

3.1 Microstructural features

The microstructural features of an as-fabricated specimen are seen in Fig. 1a. The dark circular shadows are the PMMA beads and the white spots are the particles of ZrO_2, all embedded in the matrix.

The damage modes observed on the mist surface of a fractured Group I specimen (Fig. 1b) are bead fracture and pullout, crack growth, and loosening of agglomerates of the ZrO_2 particles. The damage modes on the hackle surface of a fractured Group II specimen (Fig. 1c) are the disintegration of the matrix (through extensive void nucleation), coalescence of voids, microfracture, and decohesion between the beads and the matrix.

The microstructural features during the early stages of bending of a Group II specimen, specifically at a location where the tensile stress reached 12 MPa, are seen in Fig. 1d. There is evidence of voids at the bead–matrix interface, which may, in part, be the result of the

Fig. 1 Microstructural features of the fracture surfaces of the specimens. **a** Microstructure of an as-fabricated specimen. **b** Microstructural features of the fracture surface of Group I specimen (*mist zone*). Note bead fracture and pullout, loose agglomerates, and the mixed-mode fracture surface topography. **c** Microstructural features of the fracture surface of a Group II specimen (*hackle zone*). Note bead/matrix decohesion and void coalescence. **d** Microstructural features of a Group II specimen at the early stages of bending (12 MPa tensile stress). Note the voids at peripheral interfacial boundaries between the PMMA beads and the matrix, void coalescence, and loose agglomerates
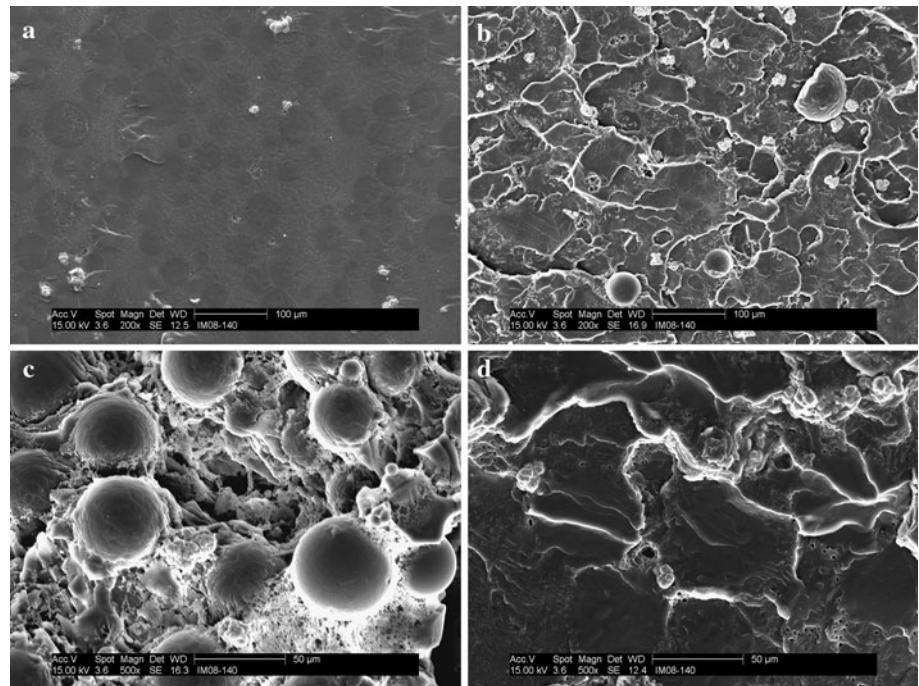
polymerization process and the acting stress. For other PMMA bone cement specimens, subjected to bending, the number of voids has been found to be directly proportional to the applied stress [28]. For a Group II specimen, at sections where the tensile stress was between 20 MPa and the fracture stress, the microstructural features include loosening of agglomerates and coalescence of voids.

3.2 Acoustic observations

The acoustic parameters measured included the quantity, amplitude, rate, and distribution of acoustic events as they evolve under increasing stress. For each value of the stress, these observations can be presented as the graph of the cumulative number of acoustic events per unit volume (cm^3) observed in each sub-interval up to the stated values of the applied stress σ plotted against the amplitude of those events. Figure 2a shows such graphs at selected stress levels for Group I specimens (under pure tension). When $\sigma < 12$ MPa, the cumulative number of acoustic events is low and nearly all have low amplitudes. At these stress levels, the main damage events are the nucleation and coalescence of voids. Since the amplitude of the acoustic signal is directly proportional to the energy released by the triggering damage event [29–32], it is inferred that the damage events releasing the least energy are in the modes of the nucleation, coalescence of voids, and initiation of other microscopic events. The continuously increasing occurrence of acoustic events with increasing amplitude corresponds to the increasing occurrence of damage modes as the local

stress becomes critical at more and more places. At ~ 12 MPa, acoustic events in the highest-amplitude sub-interval (near 90 dB) are observed for the first time.

When $12 \text{ MPa} < \sigma < 18 \text{ MPa}$, the proportion of acoustic events having large amplitudes increases, with an increasing number of them occurring in the highest-amplitude sub-interval. As a result, there is a change in the shape of the acoustic event amplitude distribution. It is inferred that many of these new acoustic events arise from new types of damage mode, which release more energy than the ones that occur below 12 MPa. Figure 1b shows (when compared with Fig. 1d) that the acoustic events taking place when $\sigma > 12$ MPa are bead decohesion, microcracks, crazing, and, eventually, widespread micro-cracking, leading to fracture of the PMMA beads and the matrix. Within the stress range $12 \text{ MPa} < \sigma < 18 \text{ MPa}$, the shape of the acoustic event amplitude distribution changes from monotonically decreasing to one with a minimum at the sub-interval with second highest amplitude.

When $\sigma > 18$ MPa, the acoustic event amplitude distribution transition is completed. Consequently, the curve in Fig. 2a shifts upward without any obvious change in shape. That is to say, although the number of acoustic events increases significantly, the distribution of their amplitudes stays the same.

It is reasonable to infer that for $18 \text{ MPa} < \sigma < 35 \text{ MPa}$, no new damage modes appear, the new damage instead having a microstructure similar to that which has already occurred (though, perhaps, at a different location in the material). In other words, in this stress range, there is no new damage formation mechanism.
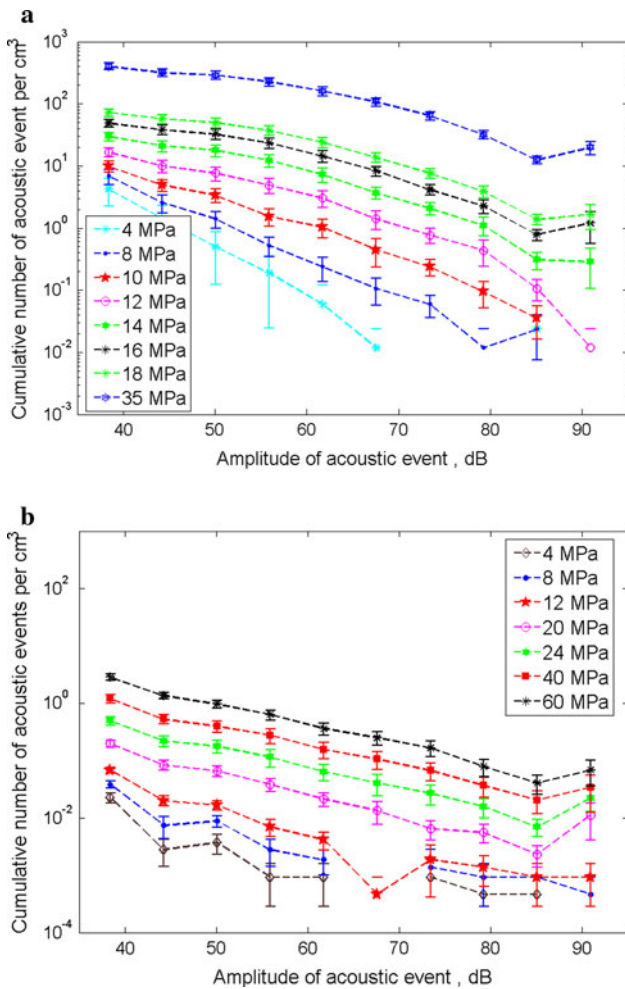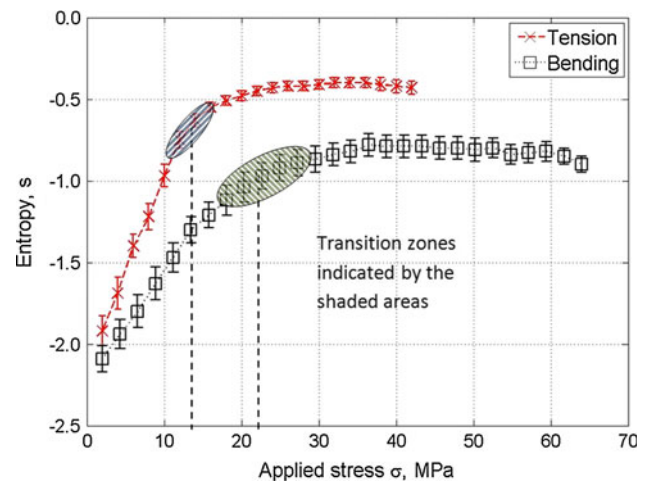
Fig. 2 Distribution of the cumulative number of acoustic signals in each of the sub-intervals under pure tension (Group I specimens) **a** and under three-point bending (Group II specimens) **b** Standard deviations are shown

Fig. 3 Variation of the approximate probabilistic entropy (s) with applied stress under tension and under three-point bending. Standard deviations are shown. In the first zone, s increases steadily; in the second (transition) zone, the rate of increase slows down; in the third zone, s is roughly constant

The results for Group II specimens are shown in Fig. 2b. The results are similar to those in Fig. 2a, but the total number of acoustic events is lower (presumably because the damage is confined to a thin layer of the specimen) and its dependence on the stress level is much weaker than under tension.

3.3 Use of s to quantify randomly generated microscopic events

Using the probabilistic entropy, the main features of the data shown in Fig. 2a or Fig 2b can be reduced to a single curve giving the empirical relationship between s and the stress σ. This is done in Fig. 3, both for tension and for bending.

Three distinct zones are seen in the s–σ relationship. In the first zone, s increases approximately linearly with applied stress ds/d$\sigma \approx$ constant > 0). This corresponds to

the increasing presence of acoustic events in sub-intervals with higher amplitudes. When detected acoustic events begin to occur in all ten sub-intervals, the s–σ curve curve bends downward, denoting the beginning of the transition zone (the second zone). This transition zone corresponds to the change in shape of the curves in Fig. 2. In the third zone, s is approximately constant (ds/d$\sigma \approx 0$), although with a slight downward curvature (d$^2 s$/d$\sigma^2 < 0$).

For the Group I specimens, the stress at the center of the transition zone (the left shaded area in Fig. 3) is ~ 12 MPa (corresponding to $\sim 30\%$ of the cement's tensile strength [33]). This stress, herein denoted the "knee-point" stress, is the stress above which, according to the foregoing results of Fig. 2, all of the damage modes become present, and below which only the less severe ones are present. For the Group II specimens, the transition takes place in a much wider acting stress level than for Group I specimens. The knee-point stress for this group is ~ 23 MPa (corresponding to $\sim 35\%$ of the cement's bending strength [34]). Whether under pure tension or bending, the completion of the shape change of the acoustic event amplitude distribution is indicated by the near maximum value of s.

4 Discussion

4.1 The characteristics of randomly generated microscopic events

For bone cement, the detected acoustic signals include characteristics of nucleation of voids, crazing, microcracking and decohesion of the beads from the MMA matrix, transgranular fracture, and pullout of beads, as well

as the order of occurrence of these damage modes, which characterize the failure mechanism of this material. These characteristics are features of the probability distribution of acoustic events which can be determined by a set of standard quasi-static tension or bending tests. The purpose of applying the stress fields in the tests is to reveal these characteristics by exciting all the possible random damage modes. One implication of these characteristics is that they could possibly foreshadow the failure of the material.

4.2 Evolution of randomly generated microscopic damage and entropy

In Fig. 4, we summarize schematically the evolution of the microscopic damage under increasing stress. The first three panels correspond to the three "zones" in Fig. 3, while the last panel represents the microstructure immediately before fracture. In the first panel, the damage is mainly sparsely localized (nucleation of voids) and the acoustic signals are mainly of low amplitude; thus, the value of s is also low. The second panel illustrates the microstructure near the knee-point stress: new and more severe damage events, such as microcracking and decohesion of the beads from the matrix, begin to take place. The amplitude distribution now includes a significantly larger proportion of high-amplitude signals and the value of s is significantly higher. The third panel illustrates the microstructure when σ is between the knee-point stress and the fracture stress. There is now widespread random damage in all of the afore-mentioned modes, but, possibly, no new modes are created, since the shape of the distribution, as shown in Fig. 2, stays roughly the same and the value of s also stays roughly the same. Note that the stress levels for both pure tension and bending at this stage, estimated according to Fig. 3 to be >20 and >30 MPa, respectively, agree well with the stress level that was theoretically predicted, by Marshall et al.

[35], at which crazes begin to form in a single-phase PMMA material, a type of self-similar meso-, micro-damage.

The fourth panel shows how the microstructure might look just before fracture occurs. New types of damage event are now taking place, including severe transgranular fracture, pullout of beads and fast microcrack propagation, leading to larger and more weakening cracks in the material and, eventually, a major fracture event. Moments before final macroscopic failure occurs, there is a small decrease in the value of s (Fig. 3). This decrease is associated with a small tendency of the acoustic events to concentrate in higher-amplitude sub-intervals (Fig. 2), suggesting an increase in the proportion of very severe damage events.

Taken together, Figs. 3 and 4 show how information about the severity of the damage may be obtained from the slope of the s–σ curve, even when the value of the applied stress is not known; specifically, the smaller the value of $ds/d\sigma$, the more severe the damage.

4.3 The transition in the s–σ curve

Note that a transition in the s–σ curve takes place when acoustic events begin to occur in all ten sub-intervals, as indicated by a decrease in the slope of the curve. The transition is complete when the shape of acoustic event amplitude distribution becomes relatively constant. Our results suggest that the underlying physics of this transition is that, within the transition zone, all possible modes of the randomly generated microscopic events are present. The presence of these modes prepares or facilitates widespread randomly generated microscopic events without the significant occurrence of new damage modes.

Interestingly, the knee-point stress, under pure tensile loading ($\sim$ 12 MPa), is approximately the fatigue limit of

Fig. 4 Schematic presentation of the evolution of random damage, under tensile stress. The *black dots* represent voids; the *red circles* represent PMMA beads firmly attached to the matrix; the *pink circles* are beads partly separated (along the *black arcs*) from the matrix. The thick *black lines* represent fractures of the matrix or of the beads
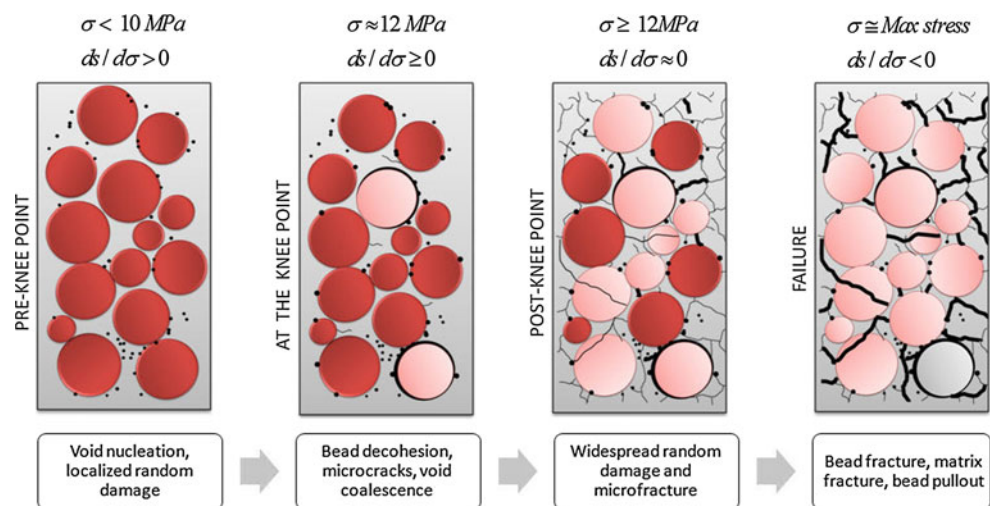
bone cement brands with compositions similar to that of the VersaBond^{TM}, as estimated from results obtained under fully-reversed tension–compression loading; specifically, 10 MPa for CMW^{TM} [34], 9.2–16.0 MPa for Cemex® [36–38], and 8.8–13.8 MPa for Palacos®R [13, 38]. The fatigue limit of CMW^{TM}, under three-point bending, has been estimated to be 20 MPa [39], a value that is again approximately the knee-point stress under three-point bending ($\sim$ 23 MPa). It is not yet clear whether these agreements exist in other materials, but it explains the effect of RGME on material fatigue performance. This finding has a great practical potential and deserves further investigation.

5 Conclusions

(1)   We characterized the randomly generated microscopic events under pure tension and under three-point bending based on the measurements of acoustic events from specimens of a quasi-brittle biomedical polymer (VersaBond^{TM} bone cement), and determined the probability distribution of the event amplitudes.

(2)   According to RGME amplitude distributions, probabilistic entropy was computed, from which an empirical relationship between s–σ was established. This relationship summarizes the activities of randomly generated microscopic events under Mode I stress and reveals that the number of different damage modes present increases with stress when ds/d$\sigma > 0$, whereas that number decreases when ds/d$\sigma < 0$. When ds/d$\sigma \approx 0$, no new random damage modes occur.

(3)   In the s–σ curve, there exists a transition zone, with the stress at the center of that zone (the "knee point" stress) corresponding to $\sim$ 30 and $\sim$ 35% of the cement's tensile and bending strengths, respectively.

References

1.   Kramer EJ. Craze fibril formation and breakdown. Polym Eng Sci. 1984;24:761–9.

2.   Huang NC, Korobeinik MY. Interfacial debonding a spherical inclusion embedded in an infinite medium under remote stress. Int J Fracture. 2001;107:11–30.

3.   Argon AS, Salama MM. Growth of crazes in glassy polymers. Philos Mag. 1977;36:1217–34.

4.   Bucknall CB. New criterion for craze initiation. Polymer. 2007;48:1030–41.

5.   Koenczoel L, Hiltner A, Baer E. Crazing and fracture in polystyrene studied by acoustic emission. J Appl Phys. 1986;60:2651–4.

6.   Feng XQ, Li JY, Yu SW. A simple method for calculating interaction of numerous microcracks and its applications. Int J Solids Struct. 2003;40:447–64.

7.   Kau C, Hiltner A, Baer E, Huber L. Damage processes in reinforced reaction injection molded polyurethanes. J Reinf Plast Comp. 1989;8:18–39.

8.   Orthopaedic Network News. Hip and Knee Implant Review. Orthopedic Network News. July 2008. 2008;19(3):15 http://www.OrthopedicNetworkNews.com.

9.   Topoleski LDT, Ducheyne P, Cuckler JM. A fractographic analysis of in vivo poly(methyl methacrylate) bone-cement failure mechanisms. J Biomed Mater Res. 1990;24:135–54.

10.   Topoleski LDT, Ducheyne P, Cuckler JM. Microstructural pathway of fracture in poly(methyl methacrylate) bone-cement. Biomater. 1993;14:1165–72.

11.   Murphy BP, Prendergast PJ. The relationship between stress, porosity, and nonlinear damage accumulation in acrylic bone cement. J Biomed Mater Res. 2002;59:646–54.

12.   Mann KA, Edidin AA, Ordway NR, Manley MT. Fracture toughness of CoCr alloy—PMMA cement interface. J Biomed Mater Res. 2000;38:211–9.

13.   Fritsch E, Rupp S, Kaltenkirchen N. Does vacuum-mixing improve the fatigue properties of high-viscosity poly(methylmethacrylate) (PMMA) bone cement? Comparison between two different evacuation methods. Arch Orthop Trauma Surg. 1996;115:131–5.

14.   Lewis G. Relative roles of cement molecular weight and mixing method on the fatigue performance of acrylic bone cement: Simplex®P versus Osteopal®. J Biomed Mater Res Part B: Appl Biomater. 2000;53:119–30.

15.   Ng ET, Qi G. Investigation of fatigue crack propagation behavior of bone cement by wavelet based acoustic emission analysis. Eng Fract Mech. 2001;68:1477–92.

16.   Sinnett-Jones PE, Browne M, Ludwig W, Buffie'e J-Y, Sinclair I. Microtomography assessment of failure in acrylic bone cement. Biomater. 2005;26:6460–6.

17.   Hull D. Fractography, observing, measuring, and interpreting fracture surface topography. Cambridge: Cambridge University Press; 1999.

18.   Qi G. Attenuation of acoustic emission body waves in acrylic bone cement and synthetic bone using wavelet time-scale analysis. J Biomed Mater Res. 2000;52:148–56.

19.   Qi G, et al. 3D real time methodology monitoring cement failures in THA. J Biomed Mater Res A. 2004;71:391–402.

20.   Garcimartin A, Guarino A, Bellon L, Ciliberto S. Statistical properties of fracture precursors. Phys Rev Lett. 1997;79:3202–5.

21.   Gibbs JW. Elementary principles in statistical mechanics. New York: Dover Publication; 1960;44–45, 168 .

22.   Penrose O. Foundations of statistical mechanics—a deductive treatment. New York: Dover Publication; 2005;215, 246 .

23.   Siegmann A, Kander RG. In situ acoustic emission monitoring and mechanical testing in the scanning electron microscope. J Mater Sci Lett. 1991;10:619–21.

24.   Battie A. Acoustic emission, principles and instrumentation. (Sandia National Lab, Report SAND82-2825, 1983).

25.   Dunegan HL, Harris DO, Tatro CA. Fracture analysis by use of acoustic emission. Eng Fract Mech. 1968;1:105–22.

26.   Hardy HRJ. Acoustic emission microseismic activity, volume 1: principles, techniques and geotechnical applications. UK: Taylor & Francis; 2003.

27. Qi G, Barhorst AA. On predicting the fracture behavior of CFR and GFR composites using wavelet-based AE techniques. Eng Fract Mech. 1997;58:363–85.

28. Chebrole, L. Microstructural observations of acrylic bone cement specimens subjected to stress. (Report, Materials Reliability Laboratory, Department of Mechanical Engineering, University of Memphis, Memphis, TN, USA, 2008).

29. Hamstad MA. Composite characterization techniques: acoustic emissions. US Army Mantech J. 1985;10:24–32.

30. Prosser WH. Advanced AE techniques in composite materials research. J Acoustic Emission. 1996;14:1–11.

31. Faudree M, et al. Characterization of damage and fracture processes in short fiber BMC composites by acoustic emission. J Compos Mater. 1988;22:1170–95.

32. Kander RGA. study of damage accumulation in unidirectional glass reinforced composites via acoustic emission monitoring. Polym Composites. 1991;12:237–45.

33. Qi G. Mechanical test reports. TN: Medical Acoustic Research Lab, The University of Memphis; 2007.

34. Jones B, Thomas EM, Salehi A. Mechanical, physical, and chemical properties of orthopaedic bone cement, Transactions of the 30th Annual Meeting of Society of Biomaterials (Memphis, TN, USA, April 27–30, 2005).

35. Marshall GP, Culver LE, Williams JG. Craze growth in polymethylmethcraylate: a fracture mechanics approach. Proc Roy Soc Lond A. 1970;319:165–87.

36. Bialoblocka-Juszczyk E, Baleani M, Cristofolini L, Viceconti M. Fracture properties of an acrylic bone cement. Acta Bioeng Biomech. 2008;10:21–6.

37. Baleani M, Cristofolini L, Minari C, Toni A. Fatigue strength of PMMA bone cement mixed with gentamicin and barium sulphate vs pure PMMA. Proc Inst Mech Eng. 2003;217:9–12.

38. Murphy BP, Prendergast PJ. On the magnitude and variability of the fatigue strength of acrylic bone cement. Int J Fatigue. 2000;22:855–64.

39. Zimmer. Cementing confidence. 2009. http://www.zimmer.com.